NANO LETTERS

pubs.acs.org/NanoLett Letter

Realizing High Utilization of High-Mass-Loading Sulfur Cathode via Electrode Nanopore Regulation

Shuibin Tu,[§] Zihe Chen,[§] Bao Zhang,[§] Xiancheng Wang, Renming Zhan, Chenhui Li, and Yongming Sun*

Cite This: *Nano Lett.* 2022, 22, 5982−5989 Read Online

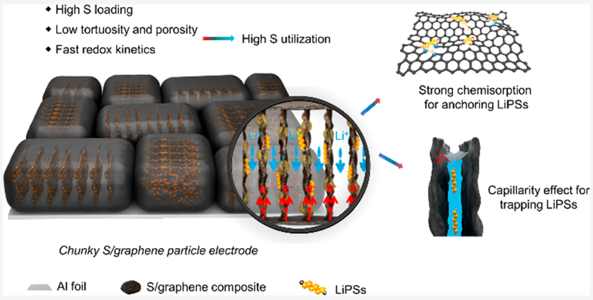

ABSTRACT: One main challenge of realizing high-energy-density lithium−sulfur batteries is low active materials utilization, excessive use of inert components, high electrolyte intake, and mechanical instability of high-mass-loading sulfur cathodes. Herein, chunky sulfur/graphene particle electrodes were designed, where active sulfur was confined in vertically aligned nanochannels (width ∼12 nm) of chunky graphene-based particles (∼70 μm) with N, O-containing groups. The short charge transport distance and low tortuosity enabled high utilization of active materials for high-mass-loading chunky sulfur/graphene particle electrodes. The intermediate polysulfide trapping effect by capillary effect and heteroatoms-containing groups, and a mechanically robust graphene framework, helped to realize stable electrode cycling. The as-designed electrode showed high areal capacity (10.9 mAh cm^{-2}) and high sulfur utilization (72.4%) under the rigorous conditions of low electrolyte/active material ratio (∼2.5 μL mg^{-1}) and high sulfur loading (9.0 mg cm^{-2}), realizing high energy densities (520 Wh kg^{-1}, 1635 Wh L^{-1}).

KEYWORDS: *lithium−sulfur batteries, nanopores, charge transport, active material utilization, energy density*

Lithium−sulfur (Li−S) batteries are considered as one of the most promising candidates for next-generation rechargeable batteries because of their high theoretical energy density (2600 Wh kg^{-1}), low cost, and abundant natural resource of S.[1−5] However, the practical implementation of Li−S batteries is plagued with several severe issues, including the insulating characteristic of S and its discharge product (lithium sulfide, Li_2S/Li_2S_2), shuttle effect caused by the soluble intermediate products (lithium polysulfides, LiPSs), and large volume change from S to Li_2S/Li_2S_2.[6−9] These issues result in low active material utilization and inferior cycling stability, especially for high-mass-loading, high-compaction-density S-based electrodes with long charge transport distance and poor mechanical stability due to their large thickness.[10−14] Nanostructured host materials with various morphologies/compositions have been designed to enhance electronic/ionic conductivity and increase S utilization of the electrodes.[15−25] For example, mesoporous carbon nanomaterials or their combination with transition metal oxides/sulfides/carbides have been investigated as S hosts, demonstrating a remarkable improvement in the electrochemical performance.[18−23] However, these electrodes usually required a high electrolyte/active materials ratio (E/AM, usually >15 μL mg^{-1}) and possessed large porosity, causing the practical energy density of Li−S batteries even lower than the state-of-the-art lithium-ion batteries (Figure S1a).

Rational design of high-loading S cathodes with low porosity and high S utilization is a feasible approach to realizing high energy density of Li−S batteries.[26−28] Figure S1b shows the theoretical computation for the relationship between energy density and porosity of the S cathode. It was found that both gravimetric energy densities (E_g) and volumetric energy densities (E_v) of the S cathodes showed a linear negative correlation with their porosity. For example, when the electrode porosity decreased from 70% (for the most reported S cathodes) to 40%, the corresponding E_g and E_v would be increased by 1.9 and 2.0 times due to the minimization of the E/AM value and electrode thickness. However, the regular electrodes fabricated via the tape casting method possess random pore geometry with high tortuosity, and poor ionic transport capability of compacted electrodes with low porosity and reduced charge transport pathways (Figure S2), leading to slow S conversion kinetics, low active materials utilization, and thus low overall capacity.[29,30] Thus, it is necessary to regulate the pore geometry and charge transfer of the compacted S

Received: June 5, 2022
Revised: July 6, 2022
Published: July 11, 2022

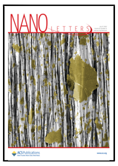

https://doi.org/10.1021/acs.nanolett.2c02258
Nano Lett. 2022, 22, 5982−5989

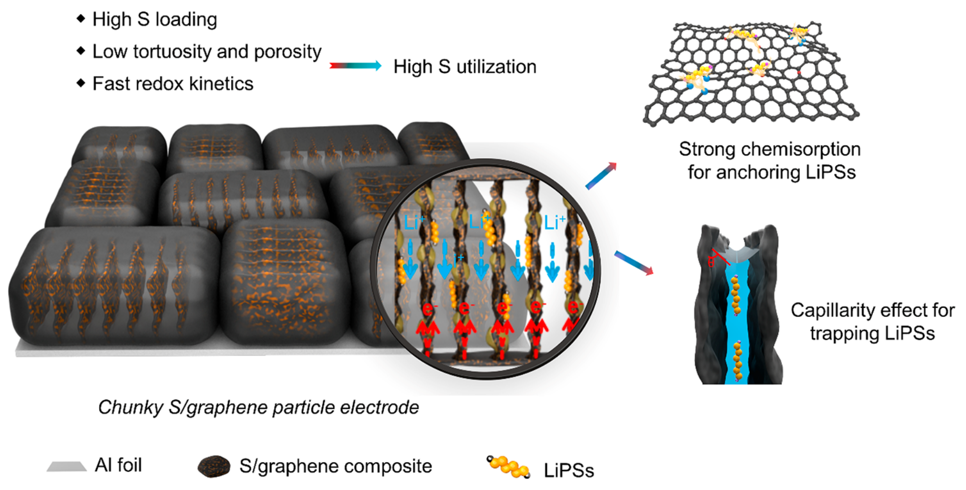

Figure 1. Schematic illustration of chunky S/graphene particle electrode with low-tortuosity internal nanochannels for rapid ionic diffusion and short conductive pathways for fast electronic transport. The strong capillary effect and chemisorption of chunky particles restrict LiPSs within the nanochannels.

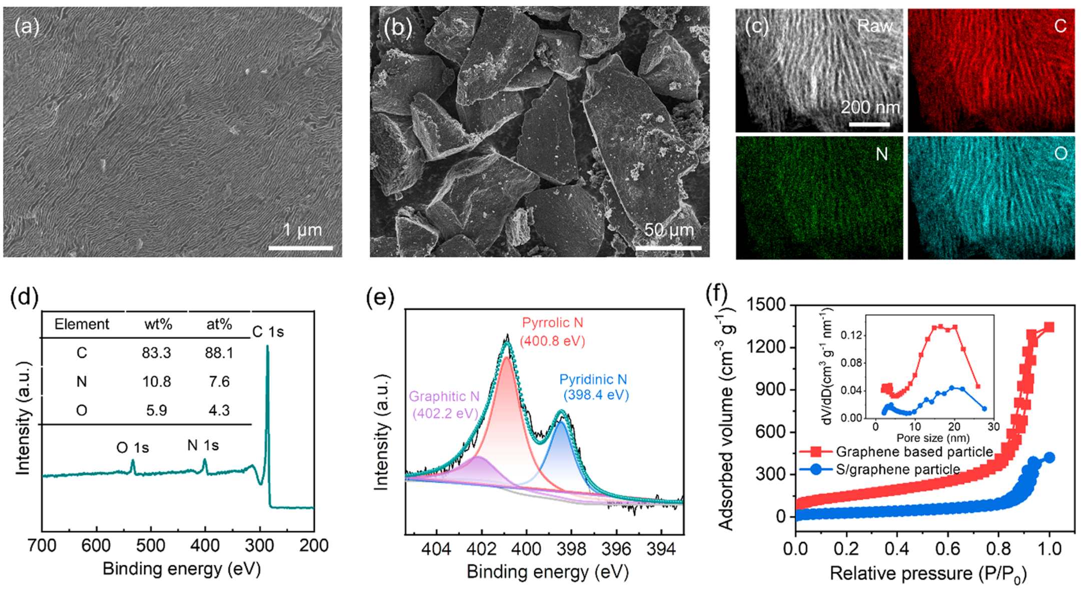

Element	wt%	at%
C	83.3	88.1
N	10.8	7.6
O	5.9	4.3

Figure 2. (a−c) SEM images (a, b) and elemental distribution mapping images (c) of chunky graphene-based particles. (d, e) XPS survey spectrum (d) and high-resolution N 1s XPS spectrum (e) of chunky graphene-based particles. (f) Nitrogen adsorption/desorption isotherms of chunky graphene-based and S/graphene particles.

cathode to realize high active material utilization at the high-mass-loading condition for high-energy-density Li−S batteries.

Here, we proposed the rational design of chunky S/graphene particle electrodes with inner Li^+ transfer nanochannels and electronic conducting pathways perpendicular to the current collector to achieve high-performance S cathodes (Figure 1). As a demonstration, we fabricated a chunky S/graphene particle electrode with a S loading of ~9.0 mg cm^{-2}, featuring active S confined in vertically aligned graphene nanochannels (width ~12 nm) with high heteroatoms content (11.9 at%) of chunky particles. The strong chemisorption capability and capillarity effect of the graphene nanochannels helped to trap LiPSs and regulate Li_2S deposition. The S/graphene particle electrode showed a high active material utilization of 72.4% with a capacity of 10.9 mAh cm^{-2} under a low E/AM value of ~2.5 μL mg^{-1}, achieving a high E_g of 520 Wh kg^{-1} and E_v of 1635 Wh L^{-1}, as well as stable cycling. The as-proposed design addressed the sluggish ion transport problem for low-porosity high-mass-loading S electrodes and thus is promising for practical high-energy-density Li−S chemistry.

The chunky graphene-based particles with the aligned pore structure were first synthesized before preparing chunky S/graphene particle electrodes (Figure S3; details can be found in the Experimental section). During the fabrication, the oxidant agent (ammonium persulfate) was rapidly added to the reaction solution after ultrasonication, triggering the rapid polymerization reaction of aniline, which simultaneously assembled with silica (SiO_2) on the surface of graphene oxide (GO) nanosheets to form GO|SiO_2@polyaniline (PANI)|GO particles. The chunky graphene-based particles were finally obtained after processing of dopamine coating, carbonization, and etching of SiO_2. The result of scanning electron microscopy (SEM) images verified the large particle size of the chunky graphene-based particles (~70 μm), much larger than the widely reported S host materials. These chunky particles were composed of paralleled graphene nanosheets

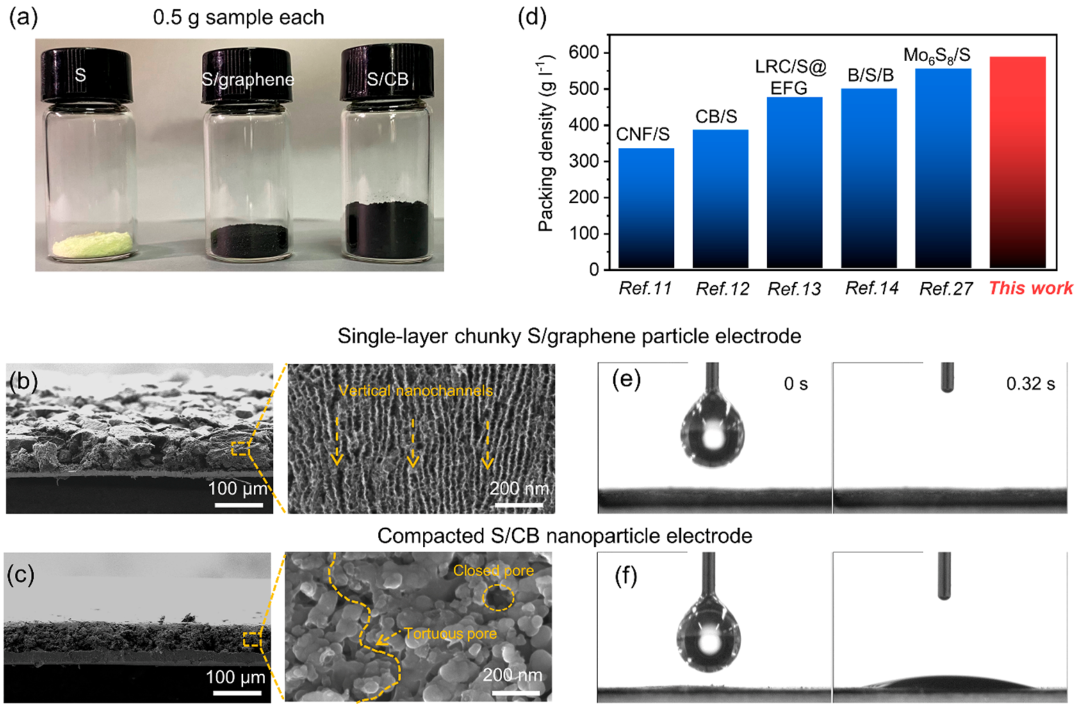

Figure 3. (a) A visual packing density comparison of pure S, chunky S/graphene and S/CB powders. (b, c) Cross section SEM images of single-layer chunky S/graphene particle electrode (b) and compacted S/CB electrode (c). (d) Comparison of the S packing density between this work and previous reports. (e, f) Electrolyte permeability test of chunky S/graphene particle electrode (e) and compacted S/CB nanoparticle electrode (f).

linked by hard carbon and had aligned nanopores with a size of ~12 nm between the graphene-based nanosheets (Figure 2a, b). The thickness of the carbon shell derived from dopamine was ~20 nm (Figure S5). Such a chunky particle design can efficiently enhance the packing density of active particles and volumetric capacity of the electrodes, and also offer continuous conductive paths for ionic/electronic transport. The elemental maps revealed the uniform distribution of carbon, nitrogen, and oxygen elements in the chunky graphene-based particles (Figure 2c), where the nitrogen and oxygen stemmed from PANI and GO, respectively. The result of the X-ray photoelectron spectroscopy (XPS) showed the atomic percentage of 88.1, 7.6, and 4.3 at% for carbon, nitrogen, and oxygen in the chunky graphene-based particles, respectively (Figure 2d). The high content of heteroatoms (11.9 at%) and their chemical states was beneficial for enhancing the performance of the S cathode.[19] As shown by the N 1s XPS spectrum (Figure 2e), the nitrogen atom existed with the forms of pyridinic N (~398.4 eV), pyrrolic N (~400.8 eV), and quaternary N (~402.2 eV),[6] providing abundant active sites to trap LiPSs and regulate the deposition of Li_2S/Li_2S_2.[31,32] The Brunauer−Emmett−Teller (BET) surface area of the chunky graphene-based particle was 515.9 m^2 g^{-1}, and its pore volume was 2.19 cm^3 g^{-1}, respectively (Figure 2f). The corresponding pore size distribution was calculated from the adsorption isotherm using the Barrett−Joyner−Halenda (BJH) model, and an average pore size of 12 nm was confirmed for the chunky graphene-based particles, which was similar to the size of the SiO_2 template. S was impregnated into the chunky graphene-based particles by a melt-diffusion process, which was denoted as S/graphene particles. The result of X-ray diffraction (XRD) measurement showed that no crystalline S signal was detected (Figure S9), indicating the complete filling of S in the nanochannels of the chunky graphene-based particles. The specific surface area and pore volume of the chunky S/graphene particles were reasonably reduced (111.3 m^2 g^{-1} and 0.67 cm^3 g^{-1}, respectively) in comparison to the initial chunky graphene-based particles. The remnant nanopore could serve as pathways for ion diffusion and accommodate the strain during the conversion between S and Li_2S/Li_2S_2. The S content in the chunky S/graphene particles was ~65.7 wt % (Figure S10).

To demonstrate the advantage of chunky S/graphene particle design in packing density, we visually compared the packing density of S, chunky S/graphene, and S/carbon black (CB) powders that was widely investigated in Li−S batteries in Figure 3a. The height of the chunky S/graphene powder was close to that of pure S powder (~800 mesh), and ~2 times larger than that of same-mass S/CB powder in the same vial, indicating its much higher packing density. Thus, low-porosity electrodes can be realized using such a chunky S/graphene powder. For example, a single-layer chunky S/graphene particle electrode with a S loading of ~4.1 mg cm^{-2} was prepared through a traditional doctor blading coating process. The thickness of the single-layer chunky S/graphene particle electrode was ~70 μm (Figure 3b), corresponding to a compaction density of ~1.1 g cm^{-3} (based on the total loading of materials on Al foil) and porosity of ~41%. During the slurry casting process, most chunky S/graphene particles lied down with the internal graphene-based nanosheets and nanochannels vertically to the Al foil, resulting in a low-tortuosity electrode architecture that allows rapid electronic/ionic transport (Figure 3b). As a comparison, with the same porosity and S loading, a compacted S/CB nanoparticle electrode was fabricated and it displayed random pore structures involving tortuous and "closed" pores (Figure 3c),

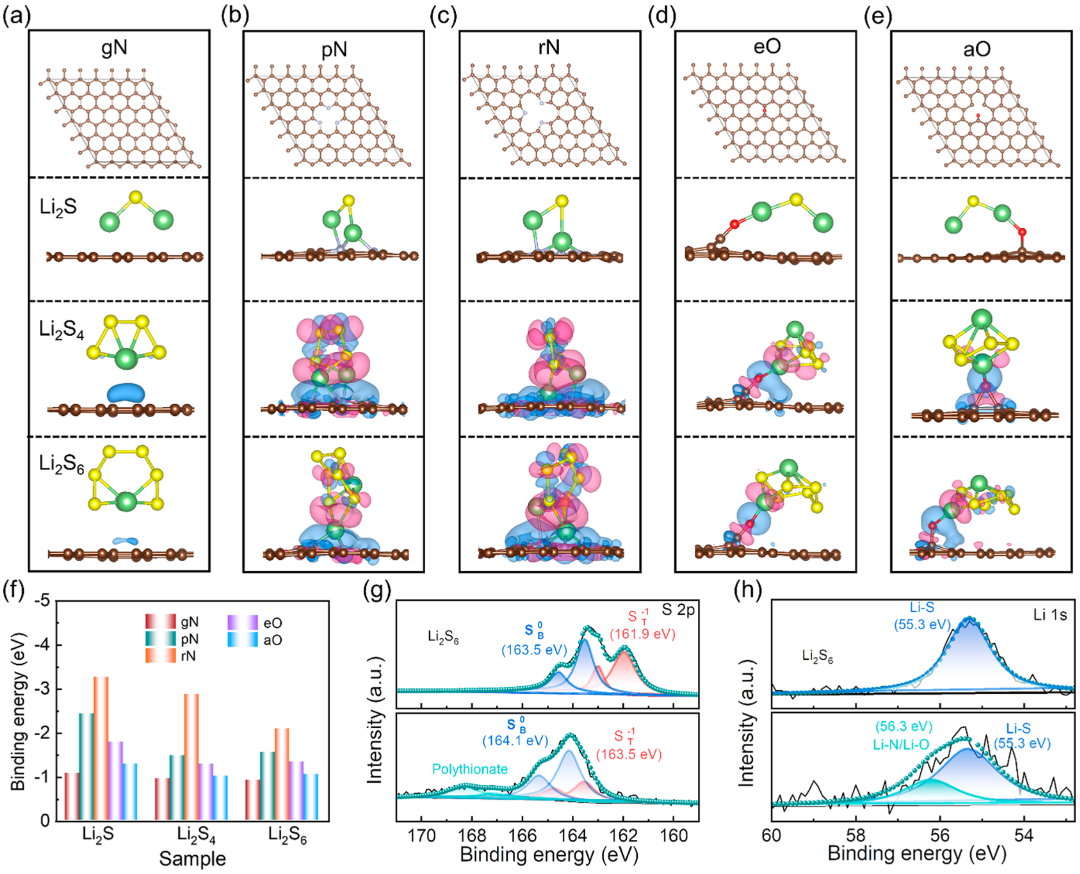

Figure 4. (a−e) The optimized structures of gN (a), pN (b), rN (c), eO (d), and aO (e) adsorbed with Li_2S, Li_2S_4, and Li_2S_6. The carbon, nitrogen, oxygen, sulfur, and lithium are marked with brown, pink, red, yellow, and green. (f) The summary of binding energies between the nitrogen and oxygen elements with LiPSs. (g, h) High-resolution S 2p and Li 1s XPS spectra before and after the adsorption of Li_2S_6.

which caused sluggish S redox kinetics. Figure 3d showed the comparison of compaction density of chunky S/graphene particle electrodes and the typical reported nanostructured or 3D structured S electrodes. The compaction density of S in the chunky S/graphene particle electrode reached 586 g L^{-1}, much higher than those nanostructured or 3D structured S electrodes (mostly <500 g L^{-1}), indicating the superiority of the chunky S/graphene particle electrode design in high E_v. To demonstrate the advantage of chunky S/graphene particle electrodes on electrolyte permeability, 4 μL of electrolyte were dropped onto a 10 mm disk electrode. The electrolyte was completely absorbed by the chunky S/graphene particle electrode within 0.32 s due to the capillary effect of perpendicular nanochannels within the chunky graphene-based particles (Figure 3e), which played an important role in enhancing S conversion kinetics. In contrast, a residual droplet was observed on the compacted S/CB nanoparticle electrode after 0.32 s and it could not be absorbed due to the distorted pore structures (Figure 3f). The capillary effect of the particles on the electrolyte can be determined by the Young−Laplace equation:

$$\rho g h \times \sin\theta = 2\gamma \times \cos\alpha / R$$

where ρ represents the electrolyte density (~0.97 × 10^3 kg m^{-3}), g is the gravimetric acceleration (9.8 m s^{-2}), h stands for the height of electrolyte in chunky graphene-based particle attributed to the capillary force attraction, θ is the angle between the nanochannels in the chunky S/graphene particle and current collector (maximum 90°), γ is the interfacial tension of electrolyte (40.8 × 10^{-3} mN m^{-1}), α is the wetting angle of electrolyte on chunky S/graphene particle electrode, and R stands for the width of half of the nanochannels in graphene-based particles. In this study, α was 25° according to the angle test (Figure S13) and R was 6 × 10^{-9} m. Therefore, the minimum value of h was calculated to be ~1.3 km, which was much higher than the real height of the nanochannels within chunky S/graphene particles (~70 μm), suggesting the superb capillary effect that could absorb the electrolyte or LiPSs solution within the chunky graphene-based particles.

In addition to the capillary effect, the heteroatoms (11.9 at %) in graphene-based particles could also endow chunky S/graphene particle electrodes with good anchoring ability to LiPSs and lithium sulfides. Density functional theory (DFT) calculations were conducted to evaluate the chemisorption ability of heteroatoms to LiPSs and lithium sulfides using Li_2S, Li_2S_4, and Li_2S_6 as the samples (Figure 4a−e). In contrast to the low binding energies of −1.07, −0.92, and −0.95 eV between graphite carbon (gN) and Li_2S, Li_2S_4, and Li_2S_6, respectively, the heteroatoms, including pyridinic nitrogen- (pN), pyrrolic nitrogen (rN), epoxy group (eO), and carboxylic group (aO) in graphene-based particles provided much higher binding energies. Especially, the rN exhibited the highest binding energies of −2.09, −2.87, and −3.26 eV with Li_2S, Li_2S_4, and Li_2S_6, respectively (Figure 4f). The strong LiPSs affinity of graphene-based particles was further confirmed by visualization experiments. The graphene-based powders were steeped into the Li_2S_6 solution. After 24 h of rest, the yellow solution became almost colorless, implying an

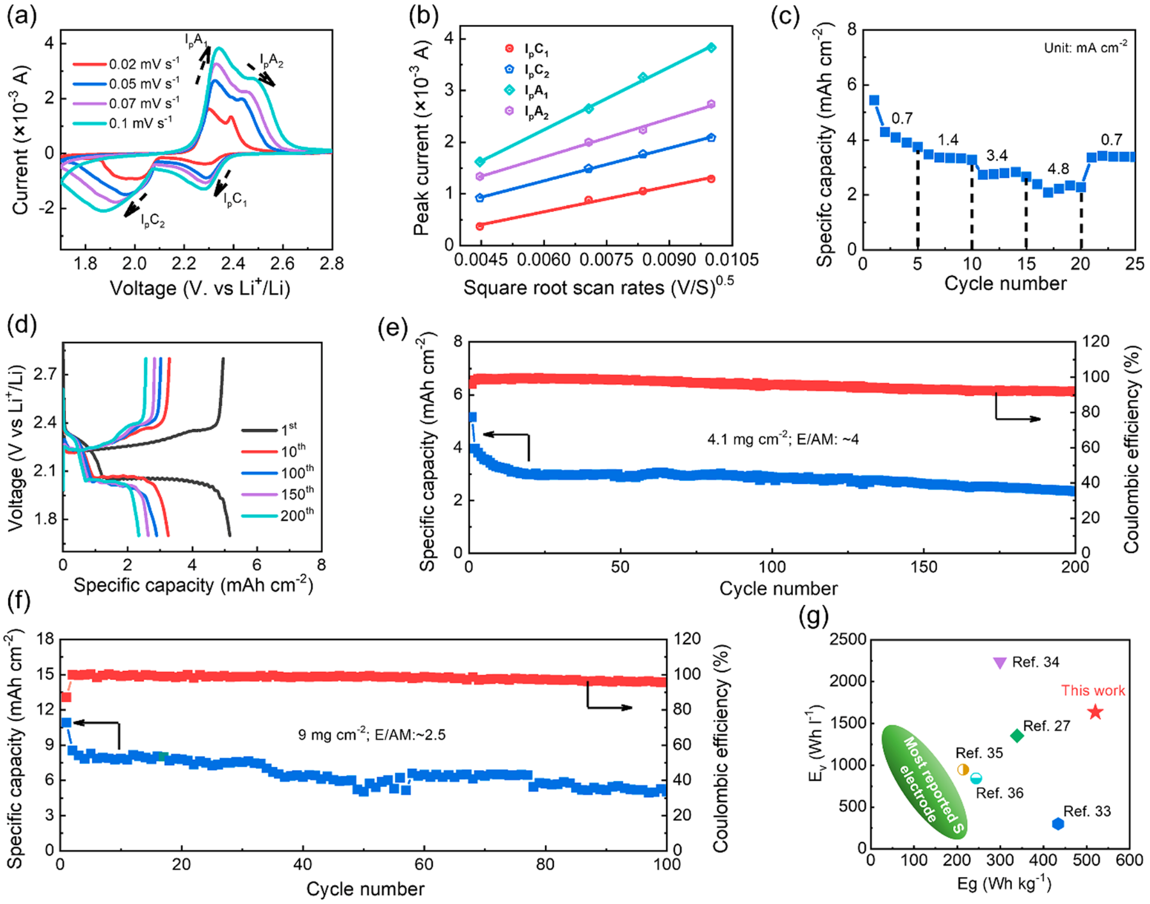

Figure 5. (a, b) CV curves of chunky S/graphene particle electrode with S loading of ~4.1 mg cm^{-2} at various scan rates (a), and corresponding relationship between the square root of the scan rate $v^{0.5}$ and the peak current I_{peak} (b). (c−e) Rate performance (c), galvanostatic charging/discharging profiles (d), and cycling performance of chunky S/graphene particle electrodes with S loading of ~4.1 mg cm^{-2} and an E/AM value of ~4 μL mg^{-1} at 1.4 mA cm^{-2} (e). (f) Cycling performance of chunky S/graphene particle electrode with S loading of ~9.0 mg cm^{-2} and an E/AM value of ~2.5 μL mg^{-1} at 1.5 mA cm^{-2}. (g) The comparison of the energy densities of S electrodes based on our data and representative publications.

excellent absorptivity of graphene-based particles to detach LiPSs from the working electrolyte (Figure S14). The Li_2S_6-absorbed graphene-based particles were analyzed using XPS. In the high-resolution S 2p XPS spectra (Figure 4g, h), no peaks for thiosulfate were detected, indicating that the samples were well protected without oxidization. The S 2p XPS spectrum of pristine Li_2S_6 could be dissociated into two peaks at 161.9 and 163.5 eV, which originated from the terminal S (S_T^{-1}) and bridging S (S_B^0) atoms, respectively.[17] Two peaks at 55.3 and 56.3 eV in Li 1s XPS spectrum of Li_2S_6-absorbed graphene-based particles were attributed to the Li−S bonds and Li−N/Li−O interaction between Li_2S_6 and graphene-based particles, respectively.[13] The S_T^{-1} and S_B^0 peaks in the S 2p XPS spectrum of Li_2S_6-absorbed graphene-based particles showed an obvious shifting to higher binding energies, which was ascribed to the decrease in electron cloud density in the S atoms.[5] These results indicated that the graphene-based particles could effectively trap LiPSs through chemisorption.

Cyclic voltammetry (CV) measurements were performed at different scanning rates with the range from 0.02 to 0.1 mV s^{-1} to investigate the Li$^+$ diffusion dynamics of the chunky S/graphene particle electrode with a S loading of ~4.1 mg cm^{-2} and a low E/AM value of ~4 μL mg^{-1}, which was much lower than those in the most reported publications (e.g., >7 μL mg^{-1}). The CV curves in Figure 5a exhibited typical S redox peaks, where the two cathodic peaks (C_1 and C_2) originated from the conversion reaction from elemental S to soluble long-chain LiPSs and further reduction to Li_2S_2/Li_2S, while the two anodic peaks (A_1 and A_2) corresponded to the reversible transformation from Li_2S_2/Li_2S to soluble long-chain LiPSs and element S. The corresponding peak currents had a linear relationship with the square root of scanning rates (Figure 5b), implying the conversion reaction was diffusion-limited. Therefore, the lithium-ion diffusion coefficients could be calculated by the Randles−Sevcik equation:

$$I_p = (2.69 \times 10^5) n^{1.5} A D_{\text{Li}}^{0.5} C_{\text{Li}} v^{0.5}$$

where I_p is the peak current, n is the number of transfer electrons, A is the active electrode area, D_{Li} (including $D_{\text{Li}}^{\text{IpC1}}$, $D_{\text{Li}}^{\text{IpC2}}$, $D_{\text{Li}}^{\text{IpA1}}$, and $D_{\text{Li}}^{\text{IpA2}}$) is the lithium-ion diffusion coefficient, C_{Li} is the concentration of Li$^+$ in the electrolyte, and v is the scan rate. The D_{Li} values of C1, C2, A1, and A2 peaks were calculated to be 2.1 × 10^{-7}, 3.4 × 10^{-7}, 1.2 × 10^{-6}, and 4.7 × 10^{-7} cm^{-2} s^{-1}, respectively. Such high D_{Li} was ascribed to the low pore tortuosity and excellent electrolyte permeability of the chunky S/graphene particle electrode. Galvanostatic charge/discharge measures were performed to systematically investigate the electrochemical performances of the chunky S/graphene particle electrode under lean electrolyte conditions. The rate capability of the S/graphene particle electrode with an E/AM value of ~4 μL mg^{-1} was evaluated under various current densities (Figure 5c and Figure S15). The chunky S/graphene particle electrode delivered an areal capacity of 5.2 mAh cm^{-2} and a specific capacity of 1268.3 mAh g^{-1} at 0.7 mAh cm^{-2}, suggesting high S utilization of 75.7%. When the current density increased to 1.4, 3.4, and 4.8 mA cm^{-2}, it delivered reversible capacities of 3.5, 2.9, and 2.4 mAh cm^{-2}, respectively, demonstrating the good rate performance under lean electrolyte conditions. Figure 5d showed the galvanostatic charge/discharge profiles for the chunky S/graphene particle electrodes during cycling. Typical double-plateau charging/discharging curves were presented, where the high discharge plateau at ~2.30 V was attributed to the conversion reactions from element S (S_8) to the soluble long-chain LiPSs (Li_2S_4), while the low one at ~2.07 V corresponded to the further conversion from Li_2S_4 to Li_2S. The ratio of the capacity of low discharge plateau to the capacity of high discharge plateau (Q_L/Q_H) theoretically was 3/1, which implied that most of the Li_2S_4 formed in the high voltage plateau could be completely converted to Li_2S. However, achieving the theoretical value of Q_L/Q_H was different due to the limited dynamics for charge transfer in the "liquid−solid" conversion process, especially for the lean electrolyte and low-porosity S cathodes. As such, the Q_L/Q_H value was a key parameter for evaluating the conversion kinetics of S cathodes. Impressively, a high Q_L/Q_H value of ~2.8 was achieved in the chunky S/graphene particle electrode at the first cycle with a current density of 0.7 mA cm^{-2} (Figure S16). After 200 cycles, it still delivered a high Q_L/Q_H value of ~2.4 at 1.4 cm^{-2}. Meanwhile, the polarization voltage was maintained at a stable value of ~0.2 V during the cycling. These results indicated the fast conversion kinetics of the chunky S/graphene particle electrode was realized. In contrast, the specific capacity of compacted S/CB nanoparticle electrode with a porosity of ~41% was 158.7 mAh g^{-1} at 0.7 mA cm^{-2}, showing an ultralow S utilization of 9.5%. It only exhibited the upper discharge plateau at either low (~4 μL mg^{-1}) or high (~15 μL mg^{-1}) E/AM values (Figure S17 and Figure S18) and a large number of soluble LiPSs remained in the electrodes (Figure S19), indicating its sluggish S conversion kinetics. The cell resistance and reaction kinetics of the chunky S/graphene particle electrode before and after cycling were studied by electrochemical impedance spectroscopy (EIS) (Figure S20). The semicircle in the high frequency corresponded to the charge transfer resistance (R_{ct}) at the electrode and electrolyte interface. The R_{ct} significantly decreased along with the advance of cycling, further demonstrating that the conducting network and ionic nanochannels of the electrode were well maintained during cycling. The cycling stability of the chunky S/graphene particle electrode was shown in Figure 5e. It delivered stable cycling performance with 80% capacity retention from the 10th to the 200th cycles at 1.4 mA cm^{-2}, indicating the high reversibility of the chunky S/graphene particle electrode. SEM images of cycled chunky S/graphene particle electrode and the corresponding energy-dispersive X-ray spectroscopy analysis showed the sustainability of the structure of graphene-based particle with the uniform S distribution within the electrode (Figure S21). In order to further demonstrate the superiority of the chunky S/graphene particle electrode design, the chunky S/graphene particle electrode with a higher S loading of ~9.0 mg cm^{-2} was prepared. Even at an E/AM value of ~2.5 μL mg^{-1}, it displayed a very high areal capacity of 10.9 mAh cm^{-2} at 0.75 mA cm^{-2} with the specific capacity of 1211.1 mAh g^{-1} and high S utilization of 72.4%, and stable cycling performance (Figure 5f and Figure S22). As a result, a high E_g of 520 Wh kg^{-1} and an E_v of 1635 Wh L^{-1} were realized for the as-achieved chunky S/graphene particle electrode (calculated based on the total mass of active material, binder, conductive additive, and electrolyte), representing a very high level compared with most reported S electrodes (Figure 5g).[33−36]

In summary, a chunky S/graphene particle electrode with vertical inner ionic transport nanochannels and electronic conducting pathways was designed for the high-energy-density Li−S batteries. Such an electrode architecture solved the issue of sluggish conversion kinetics in low-porosity high-mass-loading S cathodes. High active materials utilization with high areal capacity, as well as stable cycling stability, was realized for the as-fabricated chunky particle electrode under the harsh conditions of high mass loading (9.0 mg cm^{-2}), low porosity (~41%), and low E/AM value (~2.5 μL mg^{-1}), enabling a high E_g of 520 Wh kg^{-1} and E_v of 1635 Wh L^{-1} at the electrode level. It is expected that the successful design of the chunky S/graphene particle electrode with inner vertical charge transfer pathways and high compaction density evolutes into a universal strategy to achieve high active materials utilization at mass loading conditions and achieve reliable high-energy-density batteries.

■ ASSOCIATED CONTENT

Supporting Information

The Supporting Information is available free of charge at https://pubs.acs.org/doi/10.1021/acs.nanolett.2c02258.

Experimental details, theoretical calculation, SEM/TEM images, XRD pattern, TGA curve, contact angle test, XPS spectrum, digital images, EIS spectra, galvanostatic charge−discharge profiles, cycling performance (PDF)

■ AUTHOR INFORMATION

Corresponding Author

Yongming Sun − *Wuhan National Laboratory for Optoelectrons and School of Optical and Electron Information, Huazhong University of Science and Technology, Wuhan 430074, China;* orcid.org/0000-0001-8528-525X; Email: yongmingsun@hust.edu.cn

Authors

Shuibin Tu − *Wuhan National Laboratory for Optoelectrons and School of Optical and Electron Information, Huazhong University of Science and Technology, Wuhan 430074, China; Department of Materials Science and Engineering, Huazhong University of Science and Technology, Wuhan 430074, China*

Zihe Chen − *Wuhan National Laboratory for Optoelectrons and School of Optical and Electron Information, Huazhong University of Science and Technology, Wuhan 430074, China*

Bao Zhang − *Wuhan National Laboratory for Optoelectrons and School of Optical and Electron Information, Huazhong University of Science and Technology, Wuhan 430074, China;* orcid.org/0000-0003-3236-221X

Xiancheng Wang − *Wuhan National Laboratory for Optoelectrons and School of Optical and Electron Information, Huazhong University of Science and Technology, Wuhan 430074, China*

Renming Zhan − *Wuhan National Laboratory for Optoelectrons and School of Optical and Electron Information, Huazhong University of Science and Technology, Wuhan 430074, China*

Chenhui Li − *Department of Materials Science and Engineering, Huazhong University of Science and Technology, Wuhan 430074, China*

Complete contact information is available at: https://pubs.acs.org/10.1021/acs.nanolett.2c02258

Author Contributions

[§]S.T., Z.C., and B.Z. contributed equally to this work.

Notes

The authors declare no competing financial interest.

ACKNOWLEDGMENTS

This work is financially supported by the Natural Science Foundation of China (Grant No. 52072137) and the Innovation Fund of Wuhan National Laboratory for Optoelectronics of Huazhong University of Science and Technology. The authors would like to thank the Analytical and Testing Center of Huazhong University of Science and Technology (HUST) as well as the Center for Nanoscale Characterization & Devices of Wuhan National Laboratory for Optoelectronics (WNLO) for providing the facilities to conduct the characterizations.

REFERENCES

(1) Bruce, P. G.; Freunberger, S. A.; Hardwick, L. J.; Tarascon, J. M. Li−O_2 and Li−S batteries with high energy storage. *Nat. Mater.* **2012**, *11*, 19−29.

(2) Seh, Z. W.; Sun, Y.; Zhang, Q.; Cui, Y. Designing high-energy lithium-sulfur batteries. *Chem. Soc. Rev.* **2016**, *45*, 5605−5634.

(3) Liu, Y.-T.; Liu, S.; Li, G.-R.; Gao, X.-P. Strategy of enhancing the volumetric energy density for lithium-sulfur batteries. *Adv. Mater.* **2021**, *33*, 2003955.

(4) Chen, Z.; Zhang, Z.; Liu, C.; Jiang, C.; Mei, T.; Wang, X.; Qian, Y. Rational design of polar/nonpolar mediators toward efficient sulfur fixation and enhanced conductivity. *J. Mater. Chem. A* **2020**, *8*, 1010−1051.

(5) Zhou, G.; Chen, H.; Cui, Y. Formulating energy density for designing practical lithium−sulfur batteries. *Nat. Energy* **2022**, *7*, 312−319.

(6) Tu, S.; Chen, X.; Zhao, X.; Cheng, M.; Xiong, P.; He, Y.; Zhang, Q.; Xu, Y. A polysulfide-immobilizing polymer retards the shuttling of polysulfide intermediates in lithium-sulfur batteries. *Adv. Mater.* **2018**, *30*, 1804581.

(7) Li, S.-Y.; Wang, W.-P.; Duan, H.; Guo, Y.-G. Recent progress on confinement of polysulfides through physical and chemical methods. *J. Energy Chem.* **2018**, *27*, 1555−1565.

(8) Hou, L.-P.; Zhang, X.-Q.; Yao, N.; Chen, X.; Li, B.-Q.; Shi, P.; Jin, C.-B.; Huang, J.-Q.; Zhang, Q. An encapsulating lithium-polysulfide electrolyte for practical lithium-sulfur batteries. *Chem.* **2022**, *8*, 1083−1098.

(9) Zhou, G.; Yang, A.; Gao, G.; Yu, X.; Xu, J.; Liu, C.; Ye, Y.; Pei, A.; Wu, Y.; Peng, Y.; Li, Y.; Liang, Z.; Liu, K.; Wang, L.-W.; Cui, Y. Supercooled liquid sulfur maintained in three-dimensional current collector for high-performance Li-S batteries. *Sci. Adv.* **2020**, *6*, No. eaay5098.

(10) Lv, D.; Zheng, J.; Li, Q.; Xie, X.; Ferrara, S.; Nie, Z.; Mehdi, L. B.; Browning, N. D.; Zhang, J.-G.; Graff, G. L.; Liu, J.; Xiao, J. High energy density lithium-sulfur batteries: challenges of thick sulfur cathodes. *Adv. Energy Mater.* **2015**, *5*, 1402290.

(11) Qie, L.; Zu, C. X.; Manthiram, A. A high energy lithium-sulfur battery with ultrahigh-loading lithium polysulfide cathode and its failure mechanism. *Adv. Energy Mater.* **2016**, *6*, 1502459.

(12) Liu, J.; Galpaya, D. G. D.; Yan, L.; Sun, M.; Lin, Z.; Yan, C.; Liang, C.; Zhang, S. Exploiting a robust biopolymer network binder for an ultrahigh-areal-capacity Li-S battery. *Energy Environ. Sci.* **2017**, *10*, 750−755.

(13) Li, Z.; Zhang, J. T.; Chen, Y. M.; Lou, X. W. Pie-like electrode design for high-energy-density lithium-sulfur batteries. *Nat. Commun.* **2015**, *6*, 8850.

(14) Chung, S.-H.; Chang, C.-H.; Manthiram, A. Robust, ultra-tough flexible cathodes for high-energy Li−S batteries. *Small* **2016**, *12*, 939−950.

(15) Li, Y.; Wu, J.; Zhang, B.; Wang, W.; Zhang, G.; Seh, Z. W.; Zhang, N.; Sun, J.; Huang, L.; Jiang, J.; Zhou, J.; Sun, Y. Fast conversion and controlled deposition of lithium (poly)sulfides in lithium-sulfur batteries using high-loading cobalt single atoms. *Energy Storage Mater.* **2020**, *30*, 250−259.

(16) Tu, S.; Zhao, X.; Cheng, M.; Sun, P.; He, Y.; Xu, Y. Uniform mesoporous MnO_2 nanospheres as a surface chemical adsorption and physical confinement polysulfide mediator for lithium-sulfur batteries. *ACS Appl. Mater. Interfaces* **2019**, *11*, 10624−10630.

(17) Liu, X.; He, Q.; Yuan, H.; Yan, C.; Zhao, Y.; Xu, X.; Huang, J. Q.; Chueh, Y. L.; Zhang, Q.; Mai, L. Interface enhanced well-dispersed Co_9S_8 nanocrystals as an efficient polysulfide host in lithium-sulfur batteries. *J. Energy Chem.* **2020**, *48*, 109−115.

(18) Tao, X.; Wang, J.; Liu, C.; Wang, H.; Yao, H.; Zheng, G.; Seh, Z. W.; Cai, Q.; Li, W.; Zhou, G.; Zu, C.; Cui, Y. Balancing surface adsorption and diffusion of lithium-polysulfides on nonconductive oxides for lithium-sulfur battery design. *Nat. Commun.* **2016**, *7*, 11203.

(19) Tu, S.; Su, H.; Sui, D.; He, Y.; Cheng, M.; Bai, P.; Zhang, C.; Sun, P.; Wang, C.; Jiang, J.; Xu, Y. Mesoporous carbon nanomaterials with tunable geometries and porous structures fabricated by a surface-induced assembly strategy. *Energy Storage Mater.* **2021**, *35*, 602−609.

(20) Chu, R.; Nguyen, T. T.; Bai, Y.; Kim, N. H.; Lee, J. H. Uniformly controlled treble boundary using enriched adsorption sites and accelerated catalyst cathode for robust lithium-sulfur batteries. *Adv. Energy Mater.* **2022**, *12*, 2102805.

(21) Zhang, S.; Ao, X.; Huang, J.; Wei, B.; Zhai, Y.; Zhai, D.; Deng, W.; Su, C.; Wang, D.; Li, Y. Isolated single-atom Ni−N_5 catalytic site in hollow porous carbon capsules for efficient lithium−sulfur batteries. *Nano Lett.* **2021**, *21*, 9691−9698.

(22) Xiao, Y.; Guo, S.; Ouyang, Y.; Li, D.; Li, X.; He, W.; Deng, H.; Gong, W.; Tan, C.; Zeng, Q.; Zhang, Q.; Huang, S. Constructing heterogeneous structure in metal−organic framework-derived hierarchical sulfur hosts for capturing polysulfides and promoting conversion kinetics. *ACS Nano* **2021**, *15*, 18363−18373.

(23) Li, Y.; Wang, W.; Zhang, B.; Fu, L.; Wan, M.; Li, G.; Cai, Z.; Tu, S.; Duan, X.; Seh, Z.; Jiang, J.; Sun, Y. Manipulating redox kinetics of sulfur species using mott-schottky electrocatalysts for advanced lithium-sulfur batteries. *Nano Lett.* **2021**, *21*, 6656−6663.

(24) Zhong, X.; Wang, D.; Sheng, J.; Han, Z.; Sun, C.; Tan, J.; Gao, R.; Lv, W.; Xu, X.; Wei, G.; Zou, X.; Zhou, G. Freestanding and sandwich MXene-based cathode with suppressed lithium polysulfides shuttle for flexible lithium-sulfur batteries. *Nano Lett.* **2022**, *22*, 1207−1216.

(25) Han, Z.; Zhao, S.; Xiao, J.; Zhong, X.; Sheng, J.; Lv, W.; Zhang, Q.; Zhou, G.; Cheng, H.-M. Engineering d-p orbital hybridization in single-atom metal-embedded three-dimensional electrodes for Li−S batteries. *Adv. Mater.* **2021**, *33*, 2105947.

(26) Kang, N.; Lin, Y.; Yang, L.; Lu, D.; Xiao, J.; Qi, Y.; Cai, M. Cathode porosity is a missing key parameter to optimize lithium-sulfur battery energy density. *Nat. Commun.* **2019**, *10*, 4597.

(27) Xue, W. J.; Shi, Z.; Suo, L. M.; Wang, C.; Wang, Z. Q.; Wang, H. Z.; So, K. P.; Manurano, A.; Yu, D. W.; Chen, Y. M.; Qie, L.; Zhu, Z.; Xu, G.; Kong, J.; Li, J. Intercalation-conversion hybrid cathodes enabling Li-S full-cell architectures with jointly superior gravimetric and volumetric energy densities. *Nat. Energy* **2019**, *4*, 374−382.

(28) Manthiram, A.; Bhargav, A. Less pore equals more. *Nat. Energy* **2019**, *4*, 908−909.

(29) Xie, Y.; Pan, G.; Jin, Q.; Qi, X.; Wang, T.; Li, W.; Xu, H.; Zheng, Y.; Li, S.; Qie, L.; Huang, Y.; Li, J. Semi-flooded sulfur cathode with ultralean absorbed electrolyte in Li-S battery. *Adv. Sci.* **2020**, *7*, 1903168.

(30) Han, Z.; Li, S.; Xiong, R.; Jiang, Z.; Sun, M.; Hu, W.; Peng, L.; He, R.; Zhou, H.; Yu, C.; Cheng, S.; Xie, J. Low tortuosity and reinforced concrete type ultra-thick electrode for practical lithium-sulfur batteries. *Adv. Funct. Mater.* **2022**, *32*, 2108669.

(31) Yuan, H.; Zhang, W.; Wang, J.-G.; Zhou, G.; Zhuang, Z.; Luo, J.; Huang, H.; Gan, Y.; Liang, C.; Xia, Y.; Zhang, J.; Tao, X. Facilitation of sulfur evolution reaction by pyridinic nitrogen doped carbon nanoflakes for highly-stable lithium-sulfur batteries. *Energy Storage Mater.* **2018**, *10*, 1−9.

(32) Yuan, H.; Chen, X.; Zhou, G.; Zhang, W.; Luo, J.; Huang, H.; Gan, Y.; Liang, C.; Xia, Y.; Zhang, J.; Wang, J.-G.; Tao, X. Efficient activation of Li_2S by transition metal phosphides nanoparticles for highly stable lithium-sulfur batteries. *ACS Energy Lett.* **2017**, *2*, 1711−1719.

(33) Niu, L.; Wu, T.; Zhou, D.; Qi, J.; Xiao, Z. Polaron hopping-mediated dynamic interactive sites boost sulfur chemistry for flexible lithium-sulfur batteries. *Energy Storage Mater.* **2022**, *45*, 840−850.

(34) Guo, J.; Huang, Y.; Zhao, S.; Li, Z.; Wang, Z.; Shao, G.; Liu, J. Array-structured double-ion cooperative adsorption sites as multi-functional sulfur hosts for lithium-sulfur batteries with low electrolyte/sulfur ratio. *ACS Nano* **2021**, *15*, 16322−16334.

(35) Lu, Y.; Qin, J.-L.; Shen, T.; Yu, Y.-F.; Chen, K.; Hu, Y.-Z.; Liang, J.-N.; Gong, M.-X.; Zhang, J.-J.; Wang, D.-L. Hypercrosslinked polymerization enabled N-doped carbon confined Fe_2O_3 facilitating Li polysulfides interface conversion for Li−S batteries. *Adv. Energy Mater.* **2021**, *11*, 2101780.

(36) Zhou, J.; Wu, T.; Pan, Y.; Zhu, J.; Chen, X.; Peng, C.; Shu, C.; Kong, L.; Tang, W.; Chou, S.-L. Packing sulfur species by phosphorene-derived catalytic interface for electrolyte-lean lithium-sulfur batteries. *Adv. Funct. Mater.* **2022**, *32*, 2106966.